Patrick M. McGah[1]
Research Assistant
Department of Mechanical Engineering,
University of Washington,
Box 352600,
Seattle, WA 98195
e-mail: pmcgah@u.washington.edu

Daniel F. Leotta
Research Assistant
Center for Industrial and Medical Ultrasound,
Applied Physics Laboratory,
University of Washington,
Box 355640,
Seattle, WA 98195

Kirk W. Beach
Professor Emeritus
Department of Surgery,
Division of Vascular Surgery,
University of Washington,
Box 356410,
Seattle, WA 98195

James J. Riley
Professor

Alberto Aliseda
Assistant Professor

Department of Mechanical Engineering,
University of Washington,
Box 352600,
Seattle, WA 98195

A Longitudinal Study of Remodeling in a Revised Peripheral Artery Bypass Graft Using 3D Ultrasound Imaging and Computational Hemodynamics

We report a study of the role of hemodynamic shear stress in the remodeling and failure of a peripheral artery bypass graft. Three separate scans of a femoral to popliteal above-knee bypass graft were taken over the course of a 16 month period following a revision of the graft. The morphology of the lumen is reconstructed from data obtained by a custom 3D ultrasound system. Numerical simulations are performed with the patient-specific geometries and physiologically realistic flow rates. The ultrasound reconstructions reveal two significant areas of remodeling: a stenosis with over 85% reduction in area, which ultimately caused graft failure, and a poststenotic dilatation or widening of the lumen. Likewise, the simulations reveal a complicated hemodynamic environment within the graft. Preliminary comparisons with in vivo velocimetry also showed qualitative agreement with the flow dynamics observed in the simulations. Two distinct flow features are discerned and are hypothesized to directly initiate the observed in vivo remodeling. First, a flow separation occurs at the stenosis. A low shear recirculation region subsequently develops distal to the stenosis. The low shear region is thought to be conducive to smooth muscle cell proliferation and intimal growth. A poststenotic jet issues from the stenosis and subsequently impinges onto the lumen wall. The lumen dilation is thought to be a direct result of the high shear stress and high frequency pressure fluctuations associated with the jet impingement. [DOI: 10.1115/1.4003622]

1 Introduction

Arterial bypass grafting, a surgical procedure in which a length of tube is used to provide a pathway for blood flow around an arterial obstruction, is a common procedure to restore blood supply to the foot and lower leg. Arterial obstruction of a leg is called peripheral artery disease (PAD). If mild, the patient experiences leg pain after prolonged walking but not at rest (intermittent claudication). If the obstruction is severe, the patient experiences pain at rest and foot tissues may fail causing "ischemic" ulcerations. The bypass tube can be made of a synthetic material such as polytetrafluorethylene (PTFE), but a section of the greater saphenous vein is often used because of its increased durability [1]. In the thigh, only one major artery, the superficial femoral artery, carries blood from the groin to the knee, but several interconnected veins carry blood back toward the heart. Thus, harvesting one of these veins for use as an arterial conduit causes no obstruction to the return of blood to the heart.

A venous segment of appropriate size can be removed from the body and implanted next to the obstructed artery, attaching the ends to the artery proximal and distal to the obstruction. Alternatively, a venous segment lying next to the artery can be diverted for use as an arterial conduit in situ with the cut ends attached to the adjacent artery proximal and distal to the obstruction. Veins often have valves to direct blood flow toward the heart; hence, an excised vein is often "reversed" so that the valve flow direction is oriented with the arterial flow. For the in situ bypass, the valves must be stripped so that they do not block the blood flow, and any branches interconnecting the in situ vein segment with adjacent veins must be ligated. Since the distal ends of the vein and the artery are often smaller than their proximal ends, the sizes of the artery and vein at each end nearly match in the in situ case. In the reverse case, the small distal end is attached to the larger proximal end. Thus the surgeon must choose between several options in planning the bypass procedure: (1) Synthetic or vein? (2) If vein, reverse or in situ; (3) Exactly how should the proximal and distal anastomoses be formed?

PAD affects about 10 million Americans and several hundred thousand bypasses and related procedures are performed every year in the United States [2]. Despite its importance and frequency of use, the failure rate of bypass grafting remains high; up to 20% within the first year of implantation and up to 50% within 5 years [3,4]. The failure of the graft is usually due to the occlusion by stenotic lesions brought on by intimal hyperplasia (IH). Furthermore, as many as 70% of lower extremity bypass grafts require a reintervention procedure to correct stenotic lesions [1].

Based on observations from duplex imaging and from histological studies in animals, the graft will first adapt to the conditions of the arterial circulation in the first few months following surgery in a process referred to as arterialization. Although the specific mechanisms that trigger remodeling remain unclear, hemodynamic forces have been frequently cited as a key link in the re-

[1]Corresponding author.
Contributed by the Bioengineering Division of ASME for publication in the JOURNAL OF BIOMECHANICAL ENGINEERING. Manuscript received August 16, 2010; final manuscript received January 28, 2011; accepted manuscript posted February 9, 2011; published online March 23, 2011. Assoc. Editor: David A. Steinman.

modeling process. Several hypotheses have been proposed relating the hemodynamic stimuli to wall remodeling. There is an initial transient response of the vein resulting from the change in flow while in the arterial circulation; the vessel dilates in the classical nitric oxide or NO-mediated response [5]. However, unlike in normal venous conditions, the elevated pressure and shear stress persist, leading to permanent morphological changes resulting in a large increase in vein lumen cross section hypothesized to be a mechanism for renormalizing the wall shear stress [6,7]. The vein wall also thickens in a process hypothesized to be an attempt to reduce circumferential wall tension. Typically, the vein media layer thickens in response to the elevated arterial pressure [8,9]. It has also been hypothesized that a vein's capability to arterialize is positively related to graft patency [7].

However, the remodeling in the intima layer oftentimes progresses in an uncontrolled fashion (i.e., intimal hyperplasia) whereby the vascular smooth muscle cells (SMCs) proliferate, migrate into the intima, and deposit extracellular matrix [10]. The hyperplastic wall remodeling leads to stenotic lesions, which affect graft patency. Despite the fact that the exact biological mechanisms that trigger IH remain unknown, hemodynamic wall shear stress has consistently been shown to influence the outcome of the intimal thickness. Evidence in animal models have shown that the incidence of IH in grafts is inversely proportional to the wall shear stress magnitude (WSS) both in PTFE and autogenous grafts [11–14].

Circumstantial evidence suggests that both the spatial and temporal variations and not merely the magnitude of the WSS may be important in regulating remodeling. Evidence from ex vivo experiments suggests that large spatial wall shear stress gradients (WSSG) [15] or large temporal fluctuations [16,17] elicit various endothelial mechanotransduction responses. Morphological changes in the endothelium have been observed, such as loss of endothelial cellular alignment, increased proliferation rates, or migration away from disturbed flow regions. Such morphological changes are speculated to result in altered permeability and alteration of focal adhesion sites [10]. Further biochemical changes also occur in the endothelium under disturbed flow conditions, such as decreased NO production or increased platelet adhesion and leukocyte deposition, or altered endothelial gene regulation, all of which have been implicated in the development of IH [17,18]. However, evidence of a direct relationship between spatial and temporal gradients of shear stress and graft patency remains inconclusive.

Even with recent advances in Doppler ultrasound and phase-contrast magnetic resonance imaging, direct detailed measurements of in vivo hemodynamics remain challenging. Limitations in the spatial and temporal resolutions result in a high degree of uncertainty in the estimation of flow features, particularly with respect to measurements of the wall shear stress. Early discernment between normal remodeling from pathologic changes, which lead to stenosis or graft failure, also represents an ongoing challenge. A prior clinical surveillance study of morphological changes in revised peripheral vein grafts [19] showed that the grafts demonstrated a broad range of remodeling responses. Many of the grafts demonstrated significant lumen narrowing and/or stenoses postrevision. However, most stenoses were seen to regress, while only some continued to progress and required further revision. It remains difficult to relate these observed graft anatomical changes with flow-related changes.

Advances in computational fluid dynamics have provided useful tools to quantify the complex flow features and the spatiotemporal shear stress patterns resulting from surgical interventions in bypass grafts. These tools have allowed better quantification of the relationship between regions of shear stress and IH, particularly at the end-to-side anastomosis [20], both in idealized [21–24] and patient-specific geometries [25–27]. A high level of temporal and spatial resolution is obtained in flow features not attainable in either in vivo or in vitro experiments. Generally speaking, these studies have shown that some regions of low or oscillatory wall shear stress (particularly the distal anastomotic floor) correlate with regions of intimal thickening in vivo, which have been determined by histological examinations [22]. These studies have also elucidated the complex fluid dynamics inside the anastomosis. Helical vortices may be created in the distal end-to-side anastomosis as the flow travels from the proximal graft segment and into the outflow segment. A flow stagnation point (and a zone of low wall shear stress) may form on the floor of the distal end-to-side anastomotic segment. The stagnation point will oscillate due to the pulsatile nature of the graft flow and hence the anastomotic floor can be subjected to high oscillatory shear stresses.

The studies of Giordana et al. [26] and Moore et al. [25] emphasized the importance of the geometry in determining the flow features. Significant variations in the flow features and shear stresses are seen in each specific model. These variations are highly dependent on "global" geometric features, such as graft-to-host angle or graft-artery diameter ratio. To a lesser extent, flow features are dependent on "local" geometric features, such as small scale morphological changes like lumen cross-sectional area variation. The changes in flow field due to the geometric variations are often much greater than the changes due to flow rate or waveform shape.

Furthermore, the studies of Lei et al. [21] and O'Brien et al. [24] have simulated novel graft configurations. Lei et al. [21] reported that certain undesirable shear stress features, such as flow separation and high WSSG at the graft toe can be minimized with configurations and techniques such as cuffing and patching. On the other hand, O'Brien et al. [24] proposed a new design that used a bifurcating side-to-side configuration in order to reduce the floor stagnation point and reduce the volume of the toe separation. Their results indicate that WSSG at the anastomoses can be reduced with these altered graft configurations. However, these designs have yet to be implemented in a clinical setting. This fact implies the lack of consensus as to the most important mechanical factors (e.g., wall shear stress magnitude versus wall shear stress gradient), which influence the vascular pathophysiology.

In the recent study by Jackson et al. [27], the investigators were able to determine a significant, albeit modest, inverse correlation ($R^2=0.21$) in a cohort of eight patients between the initial wall shear stress (as determined from patient-specific computational hemodynamic simulations) and bypass graft intima-media thickness obtained in follow-up 9–12 months postsurgery. Large inhomogeneities of the intima-media thickness were measured along the length of the graft even for a single patient. This highlights the need to obtain detailed descriptions of the spatial distribution of the both the wall remodeling and the shear stress.

1.1 Research Objectives. Despite previous research efforts, no definitive mechanical, hemodynamic, or morphological features have been established as the link between remodeling and patency. The patient-to-patient variability of the flow features has hindered the development of quantifiable hemodynamic metrics predicting graft remodeling and patency. Direct quantification of the spatial distribution of remodeling and shear stresses have also remained elusive. With the exception of the above mentioned studies [26,27], no investigators have conducted longitudinal in vivo studies of graft remodeling in conjunction with detailed hemodynamic computations. However, on the other hand, many of the longitudinal in vivo studies [6,7,11,13,14] have used simplified relationships for computing wall shear stresses such as Poiseuille's law. However, secondary and transitional flow features, which themselves are thought to exacerbate the intimal hyperplasia [18], are obscured or lost by such simple fluid mechanical theories. Studies combining both longitudinal remodeling and detailed hemodynamic computations are needed to develop quantifiable metrics for the relationship between the in vivo remodeling and the hemodynamic alterations.

Here, we report on a longitudinal retrospective case study of remodeling over the course of a 16 month period in a revised

autogenous bypass graft. Hemodynamic simulations are performed in patient-specific geometries, which are reconstructed from 3D ultrasound. We compare the in vivo longitudinal outcomes with the computational shear stresses in order to discern relationships between mechanical stresses and the graft remodeling. Furthermore, the graft examined in this work was surgically removed to prevent failure 4 months after the third image acquisition. Therefore, the third image represents the end-stage of wall remodeling and allows us to explore the interplay between the altered hemodynamics and the pathological remodeling.

2 Methods

2.1 Patient History. A femoral to above-knee popliteal reversed saphenous vein graft was studied with imaging and Doppler ultrasound under a protocol approved by the University of Washington Human Subjects Division. At the beginning of our study, the graft had been revised 7 years after initial placement due to a stenosis formation at the site of a venous valve. The revision consisted of an endarterectomy and PTFE patch angioplasty, a technique in which the vessel is physically widened by suturing additional material (in this case PTFE) into a longitudinal incision in the vessel wall. Postoperative ultrasound scans of the revision site were performed at 1 month, 6 months, and 16 months after the patch angioplasty procedure. 20 months after the revision (four months after the third ultrasound scan), the entire graft was replaced due to restenosis at the patch angioplasty site accompanied by symptoms of increasing intermittent claudication.

2.2 Ultrasound Imaging and 3D Reconstruction. Ultrasound imaging was performed with a custom three-dimensional imaging system, which has been described in detail previously [28]. Briefly, a magnetic tracking system (Flock of Birds, Ascension Technology, Burlington, VT) provides measurements of the location and orientation of the ultrasound scanhead during the examination. The ultrasound imager (HDI 5000, Philips Medical Systems, Bothell, WA) and magnetic tracking system are interfaced with a personal computer equipped with a frame grabber board and custom software for simultaneous acquisition of the ultrasound images and the associated location data. Data acquisition is initiated by a hand switch and gated to an ECG signal. Cross-sectional images were obtained through the graft segment of interest. Imaging was performed in the power Doppler mode, with the gray-scale background image included. The 2D images were gathered at intervals of 1–2 mm along the area of interest. The ECG trigger was set to ensure that the data were gathered at the maximum velocity, which is about 200 ms after ECG systole. Doppler spectral waveforms were also taken at 5–20 mm intervals along the length of the revised segment, providing a display of blood velocity as a function of time over the cardiac cycle. All ultrasound measurements were recorded while the patient was in the supine position.

Custom software using the MATLAB programming environment (The MathWorks, Natick, MA) is used to reconstruct 3D surfaces from cross-sectional images [19,28]. Automatic color segmentation defines the boundary of the lumen on each of the 2D cross-sectional power Doppler views of the vessel. The automatic segmentation is reviewed and manually edited, if necessary. The contour points are transformed to locations in the 3D coordinate system of the magnetic transmitter by use of the position and orientation information associated with each image plane. Computer software connects the contour points to neighboring outlines to generate a 3D surface model of the vessel. Cubic B-splines are used to represent the lumen contours in the azimuthal directions. These contours are then connected in the longitudinal direction also using cubic B-splines. Tangency and curvature are enforced to be continuous between the splines. The 3D surface reconstructions of the three scans registered in a common coordinate system are shown in Fig. 1. The cross-sectional area measurements of the scans, also registered in a common coordinate system, are shown in Fig. 2.

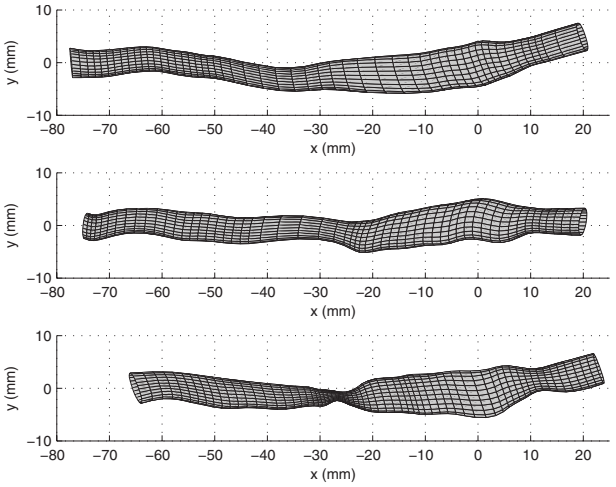

Fig. 1 Surface reconstructions of the three acquired bypass graft images registered in a common coordinate system. Reconstructions are chronological from top to bottom. Times of acquisition are 1 month, 6 months, and 16 months after a PTFE patch angioplasty. The distal patch anastomosis is used as the fiducial marker. The patch is approximately located between $x=-30$ mm and $x=+10$ mm on the top part of the reconstruction and covers about one-third of the vessel circumference.

The PTFE patch is located from about $x=-30$ mm to $x=+10$ mm in Fig. 1. The widening of the vessel indicates that the patch covers about one-third (8 mm out of the 24 mm circumference) on the top part of the images shown in Fig. 1. This was the region closest to the skin and therefore most accessible for the surgeon.

2.3 Computational Methods. The Navier–Stokes equations are solved using ANSYS® FLUENT® (Release 12.1, ANSYS, Inc., Canonsburg, PA). A second-order upwind scheme is used for the spatial discretization of the advective term in the momentum equation. Time integration is done by a second-order pressure-implicit with splitting of operators (PISO) scheme which is a type of projection method [29]. The geometries are discretized with unstructured tetrahedral cells. The mesh is generated with the package ANSYS® GAMBIT® (Release 2.4, ANSYS, Inc.). Blood is assumed to be incompressible and a Newtonian fluid with a dynamic viscosity of 3.5×10^{-3} Pa s and a density of 1050.0 kg/m^3 [30]. At the graft outlet, a stress-free condition is applied to the velocity and the pressure is fixed to zero. Rigid boundaries and the

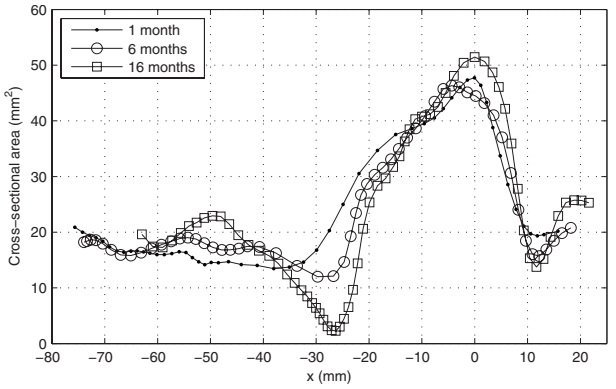

Fig. 2 Cross-sectional area measurements versus graft axis for three surface reconstructions. Coordinate system is the same as that in Fig. 1.

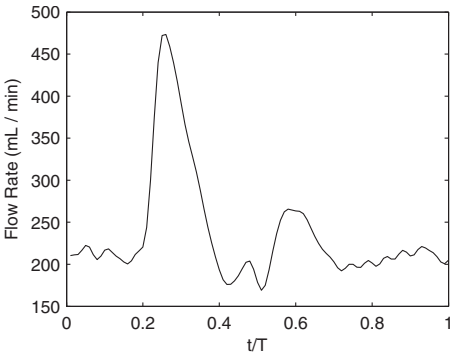

Fig. 3 Idealized volumetric flow rate applied at domain inlet (in ml/min) versus time. The time has been normalized with the period. The same waveform is used for the simulations in all three graft scans.

no-slip condition are enforced at walls.

To mimic the patient-specific flow rates, the time-dependent Womersley velocity profile is applied at the domain inlet [31]. During the ultrasound scanning procedure, measurements of the peak systolic velocities were recorded along with the shape of the centerline velocity waveform. The amplitude of the flow rate is chosen such that the peak systolic centerline velocity of the reconstructed Womersley profile is matched to the in vivo peak systolic velocity. The patient flow waveforms were recorded to have a biphasic shape. The Womersley profile is constructed from an idealized, but typical, biphasic peripheral artery waveform [32] (see Fig. 3) consisting of 24 periodic harmonic components and one mean component. The mean and peak flow rates are 237 ml/min and 473 ml/min, respectively, which are typical of lower extremity bypass graft flow rates, both with respect to the mean [7] and the peak [22] flow rate. The ECG showed that heart-rate of the patient during the scanning procedure varied from about 56–61 bpm (beat-per-minute) at 1 month, 54–58 bpm at 6 months, and 54–61 bpm at 16 months. The heart-rate were rounded to 1 s (60 bpm) for simplicity in the simulations. All three geometries are reconstructed with a circular cross section at the computational domain inlet so that the Womersley profile can be easily applied. The radius at the domain inlet in all three reconstructions is 2.81 mm. The mean Reynolds number (based on the mean flow rate and the hydraulic diameter of the vessel at the computational domain inlet) is 250 for all the three respective geometries. The peak Reynolds number (based on the maximum centerline inlet velocity and domain inlet hydraulic diameter) is 750. The Womersley number is 3.87 (based on the fundamental frequency of the heart-rate and the vessel hydraulic radius).

A series of grid resolution tests were performed to determine that sufficient spatial and temporal resolutions were used. Steady flow simulations were performed in the three geometries with a flow rate of 450 ml/min corresponding to values near systolic peak. Successive meshes were implemented with characteristic cells sizes of 0.25 mm, 0.2 mm, and 0.15 mm, corresponding to cell counts of about 0.5×10^6, 2×10^6, and 5×10^6, respectively. The volume-averaged pointwise changes in individual velocity components were less than 5% and 2% (using the mean inlet velocity as a scale) between the two mesh refinements in the first two geometries. The asymptotic values of the wall shear stress components were estimated by a Richardson exptrapolation. The surface-area-averaged pointwise errors of the shear stress components had converged to within 6% for the streamwise component and 4% for the spanwise component, using the mean shear stress at the domain inlet as a scale.

The simulations of the first two scans were carried out for five cardiac cycles. A time step of 0.0002 s, giving 5000 time steps per cardiac cycle, is chosen for stability and accuracy of the simulation according to the Courant-Friedrichs-Lewy (CFL) criterion. The first two cycles were discarded from the analysis to ensure that simulation start-up transients were eliminated. The results from all three cycles were compared and found to vary only within the noise level of the simulation. No signs of chaotic flow were observed in the first two geometries. In the simulations of the third scan, however, we found flow variables to be aperiodic, denoting chaotic behavior particularly during the decelerating portion of the systole. Therefore, an additional two cycles (five cycles excluding start-up cycles) were computed to obtain a preliminary estimate of the strength of chaotic fluctuations between cycles.

The shear stress parameters are computed via the following standard definitions. The instantaneous WSS is the absolute value of the wall shear stress vector,

$$\mathrm{WSS} \equiv |\boldsymbol{\tau}| = (\tau_m^2 + \tau_n^2)^{1/2} \tag{1}$$

where τ_m and τ_n represent the streamwise and spanwise components, respectively, of the wall shear stress vector. The time-averaged wall shear stress (TAWSS) is computed over a given cardiac cycle,

$$\mathrm{TAWSS} \equiv \frac{1}{T}\int_0^T |\boldsymbol{\tau}| dt \tag{2}$$

where T is the period of the cardiac cycle. The time integration is performed with a simple midpoint rule. The spatial WSSG is calculated by taking the spatial derivatives of the wall shear stress vector resulting in a four component tensor:

$$\nabla\boldsymbol{\tau} = \begin{bmatrix} \dfrac{\partial\tau_m}{\partial m} & \dfrac{\partial\tau_m}{\partial n} \\ \dfrac{\partial\tau_n}{\partial m} & \dfrac{\partial\tau_n}{\partial n} \end{bmatrix} \tag{3}$$

In this work, only the absolute value of the tensor is used to report the WSSG, which is the square root of the sum of the squares of all four components.

$$\mathrm{WSSG} \equiv |\nabla\boldsymbol{\tau}| = \left[\left(\frac{\partial\tau_m}{\partial m}\right)^2 + \left(\frac{\partial\tau_m}{\partial n}\right)^2 + \left(\frac{\partial\tau_n}{\partial m}\right)^2 + \left(\frac{\partial\tau_n}{\partial n}\right)^2\right]^{1/2} \tag{4}$$

The oscillatory shear index (OSI) is often used to quantify temporal variation and reversal of shear stress and has been shown to correlate with vascular regions susceptible to atherosclerotic plaques such as in the carotid bifurcation [33] or in the coronary arteries [34]. The definition of the OSI used here was first proposed by He and Ku [34],

$$\mathrm{OSI} \equiv \frac{1}{2}\left[1 - \frac{\left|\displaystyle\int_0^T \boldsymbol{\tau} dt\right|}{\displaystyle\int_0^T |\boldsymbol{\tau}| dt}\right] \tag{5}$$

The OSI is normalized so that it can only take on a value between zero and one-half. The value of the OSI is also independent of the magnitude of the shear stress.

Phase-averaging of the flow field, which represents the coherent time-varying behavior, is used to distinguish the coherent flow dynamics from chaotic or aperiodic flow dynamics. Large deviations from the phase average can be useful for identifying flow instability or flow transition. For a generic field variable, $f(x,y,z,t)$, the phase average over N cycles, denoted by $\langle f\rangle(x,y,z,t)$, is given by

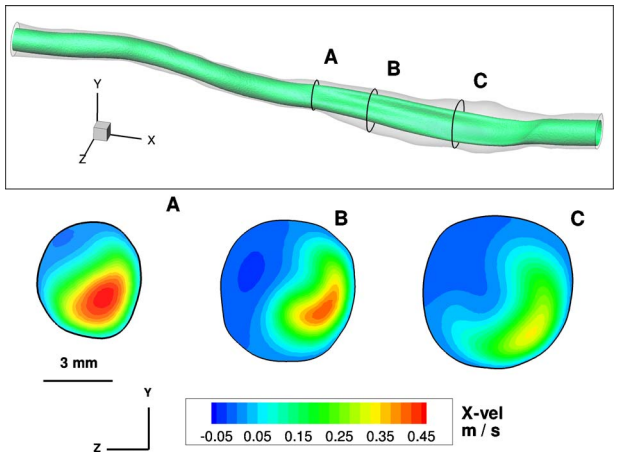

Fig. 4 Instantaneous streamwise velocity contours of the 1 month scan at time *t*/*T*=1. Top subfigure is a 3D depiction of the surface of constant *x*-velocity (0.15 m/s). (*a*)–(*c*) depict the out-of-plane velocity contours at three axial slices located at *x*=−27, −17, and −2 mm, respectively. Bar labeled 3 mm gives relative size of the three subfigures.

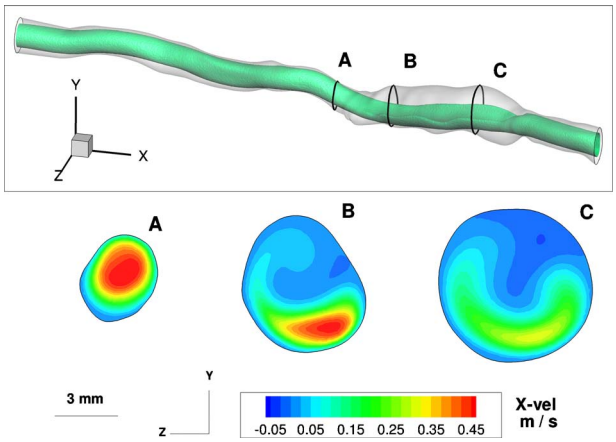

Fig. 5 Instantaneous streamwise velocity contours of the 6 month scan at time *t*/*T*=1. Top subfigure is a 3D depiction of the surface of constant *x*-velocity (0.15 m/s). (*a*)–(*c*) depict the out-of-plane velocity contours at three axial slices located at *x*=−27, −17, and −2 mm, respectively. Bar labeled 3 mm gives relative size of the three subfigures.

$$\langle f\rangle(x,y,z,t) = \frac{1}{N}\sum_{n=0}^{N-1} f(x,y,z,t+nT) \tag{6}$$

where T again represents the period of the cardiac cycle. The fluctuating or chaotic component with respect to the phase average is

$$f'(x,y,z,t) = f(x,y,z,t) - \langle f\rangle(x,y,z,t) \tag{7}$$

The root mean square (rms) value of the fluctuating component is the phase average of the mean square fluctuation. It represents a magnitude of the aperiodic fluctuations. It is defined as

$$f'_{\text{rms}} = \sqrt{\langle f'^2\rangle} \tag{8}$$

3 Results

Over the course of the three visits, the graft underwent large remodeling in two principal regions: the first region is at the proximal side of the patch where the stenosis, with over 85% in area reduction, develops. The second region is at the distal side of the patch where an expansion or poststenotic dilatation (PSD) of the vessel occurs (PSD is an expansion of the vessel downstream of a stenosis). We discuss the relevant flow features in these two regions separately. We examine low and oscillatory WSS and high WSSG near the location of the stenosis development in light of the connection of shear stress to intimal hyperplasia. Also, we examine high frequency pressure and shear stress oscillations in the poststenotic region as a possible connection to the observed poststenotic dilatation.

3.1 Stenotic Region. Proximal to the patch anastomosis, the flow is laminar for all three cases. In the first two scans (1 month and 6 months), a similar secondary flow pattern is seen at the patch anastomosis; flow separation occurs on one side of the lumen due to both curvature in the vessel and an increase in the cross-sectional area of the lumen. The flow remains separated ipsilateral to the patch for the entirety of the cardiac cycle. Based on the coordinate system from the ultrasound reconstructions, the separations occur at approximately $x=-35$ mm and $x=-26$ mm in the first and second scans, respectively (see Fig. 2). As depicted in Figs. 4 and 5, the velocity profile is skewed toward the lumen contralateral to the separation point and develops into a wall-jet flow with a "crescent moon" type velocity profile. A recirculation zone develops inside the revised region ipsilateral to the separation; there is little net forward flow. Figure 6 shows a 2D plane plotting the instantaneous streamwise velocity contours at diastole. The figure also visualizes the flow separation and recirculation zone for the scan at 1 month. The wall-jet velocity profile remains coherent and does not break down into chaotic motion throughout the entire cardiac cycle in both visits. Some destabilization of the wall-jet velocity profile is seen during the systolic deceleration (in both cases 1and 2), where two counter-rotating longitudinal vortices are seen to escape from the jet's outer shear layer. But these vortices are coherent and repeatable from cycle to cycle.

As a consequence of the flow separation and skewed velocity profile, low TAWSS is seen over the entire cardiac cycle in the recirculation region ispilateral to the separation (<0.5 Pa). Not surprisingly, the OSI in the separation region is high (>0.25). Contralateral to the separation, where the wall jet adheres to the lumen, moderate to high WSS is seen over the cardiac cycle in the first two scans due to the wall-jet. The contralateral TAWSS is approximately 2–3 Pa (the reference shear stress at the inlet by Poiseuille's law is 0.87 Pa). The OSI is likewise low along this side. Figures 7–9 show contour plots of the time-averaged WSS, OSI, and time-averaged WSSG respectively, for the three scans.

It must be emphasized that the separation and wall-jet features

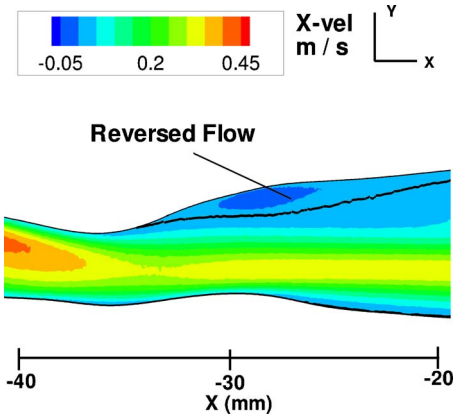

Fig. 6 Instantaneous streamwise velocity contours on a 2D plane of the 1 month scan at time *t*/*T*=1 detailing the flow separation and recirculation zone. Dark line delineates forward moving versus reversed flow. The *Z* (out-of-plane) position of the plane is in the approximate vessel center.

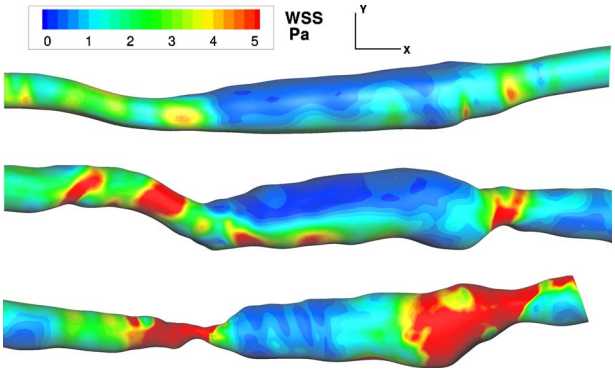

Fig. 7 Time-averaged wall shear stress contours on graft lumen for one cycle (in Pa). Scans are chronological from top to bottom and the flow is from left to right. WSS is approximately symmetrical on the backside of the lumen.

are clearly seen in both the scans at 1 and 6 months. Despite small scale morphological changes between the two reconstructions, these secondary flow features are stable, robust, and primarily determined by the global geometric configuration. Preliminary simulations with exerciselike flow conditions (mean flow rate of 375 ml/min and heart rate of 100 bpm) showed that the wall jet remained. The area exposed to low shear in the recirculation region was also reduced in size but was not eliminated.

In the third scan, the hemodynamics at the proximal revised region is markedly different from the first two scans. The stenosis

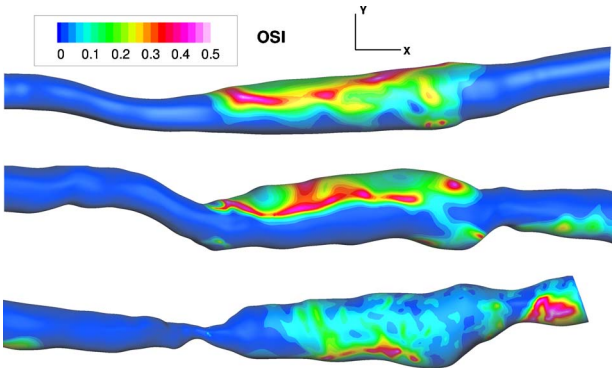

Fig. 8 OSI contours on graft lumen for one cycle. Scans are chronological from top to bottom and the flow is from left to right. OSI is approximately symmetrical on the backside of the lumen.

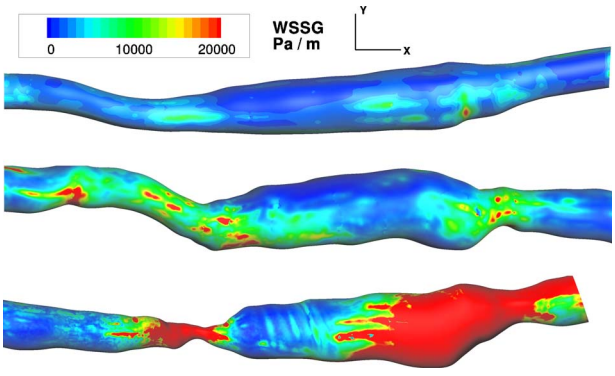

Fig. 9 WSSG contours on graft lumen averaged over one cycle (in Pa/m). Scans are chronological from top to bottom and the flow is from left to right. WSSG is approximately symmetrical on the backside of the lumen.

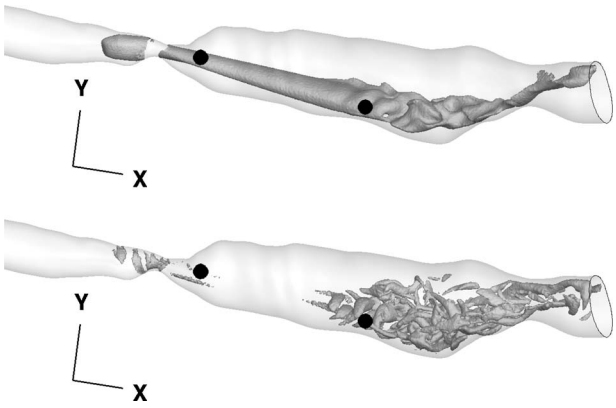

Fig. 10 Visualization of the velocity in the poststenotic jet in the 16 month scan. The time is $t/T=1$ at the end of the fifth cycle. (*a*) Instantaneous streamwise velocity isosurface (=0.50 m/s). The dots indicate the points used to measure the time histories depicted in Fig. 11(*a*) (left dot) and Fig. 11(*b*) (right dot). (*b*) Coherent vortices identified by the *Q* criterion. *Q* value is 0.3 (normalized with stenosis diameter and mean stenosis centerline velocity).

(located at $x=-27$ mm in Fig. 2) acts like a nozzle and accelerates the fluid to mean centerline velocities of ≈ 0.5 m/s and peak systolic velocities >3 m/s. This produces a poststenotic, jet which persists throughout the entire cardiac cycle. The acceleration of the fluid causes steep velocity gradients at the throat. Very high WSS values are seen over the entire cardiac cycle at the stenosis throat where the TAWSS is above 50 Pa and the instantaneous WSS reaches above 100 Pa during systole. This pathological level of shear stress would be expected to desquamate the endothelium making the lumen susceptible to platelet deposition. The rate-of-strain seen in the jet's shear layer is above 2000 s^{-1} for much of the cardiac cycle. This magnitude of strain rate may have caused additional complications such as hemolysis or platelet activation [35]. We hypothesize that the large shear stress at the stenosis is the hemodynamic mechanism, which would have triggered a thrombotic occlusion and the subsequent failure of the graft.

Indeed, these values of wall shear stress and strain rate are higher than those normally found in the healthy vasculature. However, such large values have been reported in the literature in pathophysiological situations, particularly in stenotic vessels. In numerical simulations of idealized carotid artery stenoses, Stroud et al. [36] reported a value of shear stress of 160 Pa at the throat of a 75% stenosis at peak systole (implying a wall shear rate of $\approx 40,000$ s^{-1}).

3.2 Poststenotic Dilatation. The jet coming from the stenosis in the third scan impinges onto the lumen several diameters downstream from the stenosis. The Reynolds number based on the stenosis diameter and the mean cross-sectional velocity is ≈ 850. At this high Reynolds number, the jet becomes unstable and transitions into a chaotic state. The jet is transitional for the entire cardiac cycle. In Fig. 10, a streamwise velocity isosurface (0.5 m/s) is depicted at mid-diastole.

Large spatial variability and aperiodicity are seen in the velocity and shear stress fields between cycles in the poststenotic region. We compute mean and mean square fluctuation quantities from the ensemble averaged of five cardiac cycles (once we have removed two cycles to eliminate initial transients). Since five cycles reduces the noncoherence only by a factor of $1/\sqrt{5}$, our computations may not give precise velocity statistics. However, the averaging still allows us to confirm the aperiodicity of the flow field and estimate the intensity of the fluctuations.

As we expect in this nonlinear, transitional flow, the velocity

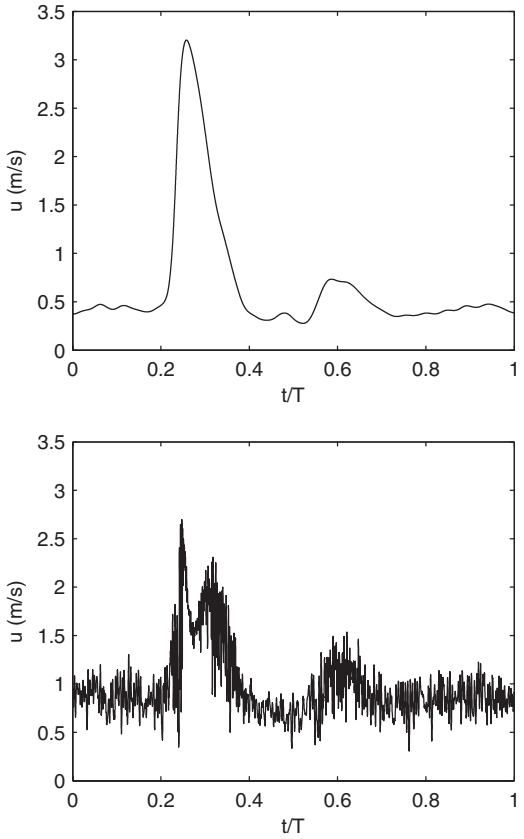

Fig. 11 Phase-averaged *x*-velocity history at two spatial points in the 16 month scan; (*a*) is at a point located near the stenosis throat and (*b*) is located in the mid-dilated region. See the dots in Fig. 10 for specific locations.

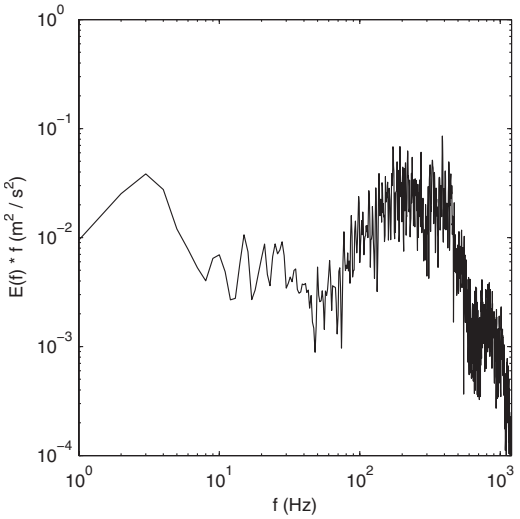

Fig. 12 Streamwise velocity power spectrum versus frequency. The velocity signal is from the 16 month scan in the poststenotic region and at the same point as given in Fig. 11(*b*). The frequency spectrum is computed from the five simulated cycles. Note the spectral energy at frequencies <10 Hz, indicating the cardiac cycle frequencies, and the energy at 100–500 Hz, indicating the jet transition.

fluctuates at high temporal frequencies, much higher than any forcing frequency. Detailed time histories of the streamwise velocity are measured at several points in the poststenotic region. Two typical phase-averaged time histories are shown in Fig. 11. The first plot is relatively smooth. The velocity power spectrum is relatively narrow and most of the energy is contained in frequencies <24 Hz. The time signal at this point is relatively repeatable, with the rms fluctuations being less than about 5%.

The second plot clearly shows high temporal velocity fluctuations. The time signal is highly aperiodic, with rms fluctuations being as high as 25%. The power spectrum of the fluctuating velocity at the second point, shown in Fig. 12, displays a broad bandwidth with significant energy in the range 100–500 Hz. Thus, although the simulation is forced at low frequencies (<24 Hz), the inherent nonlinearity of the turbulent transition feeds a transfer of energy to high frequency modes, which are much higher than any forcing frequency.

At the impingement region in the third scan, the lumen is subjected to very high WSS. The TAWSS is above 10 Pa at the dilated and the peak WSS reaches as high as 50 Pa in some locations. High spatial and temporal fluctuations are also seen in the shear stress. Root-mean-square fluctuations in the shear stress are also as high as 20%. A large value of OSI is seen in the poststenotic region near the impingement for each individual cycle (see Fig. 8). Two primary factors are associated with the high OSI values: (1) oscillations in the jet orientation as it issues from the stenosis and the resulting changes in the location of the impingement point and (2) transitional flow fluctuations. The time-averaged WSSG is $>2\times10^4$ Pa/m and local time-averaged values reach as high as 10^5 Pa/m and the peak systolic WSSG is as high as 5×10^5 Pa/m at the impingement (see Fig. 9). These are levels of shear stress where we would again expect endothelial dysfunction. This level of WSSG would imply a change in WSS of about 1 Pa over the length of a single endothelial cell ($\sim10^5$ Pa/m$\times10^{-5}$ m$=1$ Pa)! Values of this magnitude of WSSG have not been previously reported in lower extremity bypass grafts. Walsh et al. [23] reported values of WSSG $\approx$2300 Pa/m on the floor of a bypass graft's distal anastomosis. However, their reported WSSG only contains one component of the tensor, equivalent to $\partial\tau_m/\partial m$ given in Eq. (4). Our results indicate that each component of the shear stress gradient tensor is of similar magnitude in the poststenotic region. Presumably, their value of WSSG would have been much higher had all four components been computed.

It should be noted that resolution tests in the third scan were performed in addition to those described in Sec. 2. The chaotic breakdown of the poststenotic jet represents additional difficulties in ensuring that the flow field is sufficiently resolved. It is difficult to ascertain that differences between simulations are not the result of mesh dependence rather than different realizations of a chaotic process. Particular attention was given to the sensitivity of the poststenotic flow field for the three meshes (cell sizes of 0.25 mm, 0.2 mm, and 0.15 mm). Unsteady simulations were performed with a steady inlet flow rate. The test simulations were executed for a fraction of the cardiac cycle. After excluding a startup of 0.05 s, the area-averaged and time-averaged wall shear stress magnitudes were 12.42 Pa, 12.47 Pa, and 13.05 Pa. Likewise, the location of the jet impingement (as determined by a sudden increase in shear along the lumen) changed less than 3 mm, about 1.5 stenosis diameters, over the mesh refinements. Thus, we are confident that the global flow features, such as jet impingement and subsequent destabilization, and the elevated poststenotic wall shear stresses are sufficiently captured at this level of spatial resolution.

3.3 Comparisons With In Vivo Measurements. As mentioned in Sec. 2, Doppler ultrasound velocimetry was performed at different locations along the axis of the graft. Because the 3D tracker was not activated during the collection of the Doppler spectral waveforms (which were captured as part of the patient's standard clinical examination), we cannot quantitatively determine the location of the Doppler spectral recordings. However,

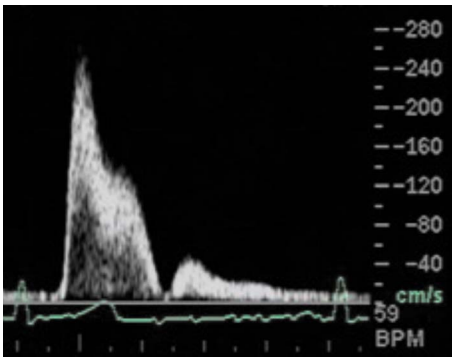

Fig. 13 In vivo Doppler ultrasound measurements of velocity at the stenosis throat for one cardiac cycle. Abscissa is the time (approximately 1 s) and ordinate is the velocity (cm/s). Compare with Fig. 11(*a*).

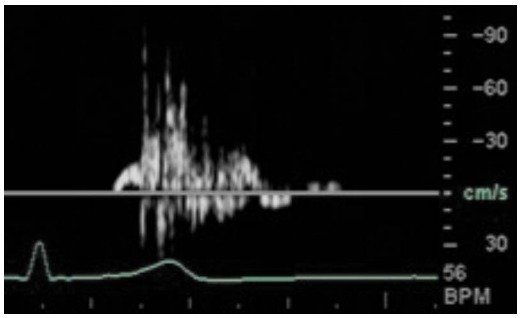

Fig. 14 In vivo Doppler ultrasound measurements of velocity near the distal graft anastomosis for one cardiac cycle. Abscissa is the time (approximately 1 s) and ordinate is the velocity (cm/s). Compare with Fig. 15.

the spatial location can be estimated by visually examining the 2D gray-scale guidance images that accompany each Doppler waveform image. Although direct quantitative comparisons between the Doppler recordings and the simulation velocities cannot be made, some qualitative statements can be made.

For the scan at 1 month, the Doppler velocimetry measured peak systolic velocities of ≈1.0 m/s in the graft a few centimeters proximal to the patch anastomosis. From the simulations, the computed peak systolic velocities in the region $x \approx -50$ to -40 mm were between 0.80 m/s and 0.85 m/s, which is a difference of about 22%. Similarly, in the scan at 6 months, the Doppler velocimetry measured peak systolic velocities ranging from 0.76 m/s to 0.85 m/s proximal to the patch anastomosis. The computed peak systolic velocities in the corresponding simulation in the region $x \approx -50$ to -40 mm were between 0.75 m/s and 0.80 m/s. In both the in vivo scans from 1 and 6 months, spectral broadening and backward flow were observed in the Doppler velocimetry measurements in the revised segment, which are indicative of secondary flows [19]. This observation would be consistent with the simulation results: the flow separation, wall jet, and recirculation in the revised region (e.g., Figs. 4 and 5).

For the last scan taken at 16 months, Doppler velocimetry recorded peak systolic velocities of ≈0.54 m/s proximal to the stenosis, while the simulation computed values of 0.51–0.55 m/s in the region $x \approx -50$ to -40 mm. At the throat of the stenosis, Doppler velocimetry recorded peak systolic velocities between 2.35 m/s and 2.71 m/s (see Fig. 13). The simulations computed peak systolic velocities at the stenosis ≈3.25–3.5 m/s (see Fig. 11(*a*)).

Doppler measurements made in the poststenotic region of the third scan also showed spectral broadening and reversed flow during systole, which again is indicative of the flow transition in the poststenotic jet. A typical in vivo velocity measurement of flow in the poststenotic region is shown in Fig. 14. In comparison, computed flow waveforms in the poststenotic region (see Fig. 15) also show high frequency fluctuations. The velocity fluctuations are strongest during systole in both the computations and the in vivo measurements, but the simulated amplitude of the oscillations is smaller than those seen in vivo.

4 Discussion

Although the simulations of the three ultrasound scans in this study are an incomplete picture of the remodeling process, they provide a valuable method to study the relation between mechanical stresses and vascular remodeling as a compliment to the in vivo ultrasound surveillance. More importantly, we can quantify the temporal and spatial variabilities of shear stress, which is not possible with current direct in vivo measurements. Interpreting our results in light of the prevailing theories of vascular remodeling, our conclusions can be summarized with the following two statements:

- The main stenosis is seen to progress in vivo proximal to the flow separation point in the patch recirculation zone. Low TAWSS and flow stagnation are seen in the graft on the ipsilateral side of the flow separation. Based on the correlation between simulated hemodynamics and observed in vivo remodeling, we present the preliminary hypothesis: *The low wall shear stress conditions distal to the flow separation resulted in an environment conducive to intimal hyperplasia that led to a severe stenosis.*
- The poststenotic dilatation of the lumen occurred in a region of elevated WSS due to the poststenotic jet impingement. We furthermore interpret this finding according to a second working hypothesis regarding the mechanism of the poststenotic dilatation: *The poststenotic lumen dilated to renormalize the high levels of WSS, possibly via an endothelial shear stress or stretch mediated pathway.*

As multiple shear stress parameters (low WSS, high OSI, and high WSSG) are seen at the proximal patch anastomosis, it is not easily discernible which factor is the primary culprit. Nor is it possible to make independent measurements in our current work between the shear stress parameters and the vessel growth and remodeling. Given that the stenosis is seen to progress in vivo on the proximal side of the flow separation, with additional lumen narrowing seen on the distal side of the separation, the low shear

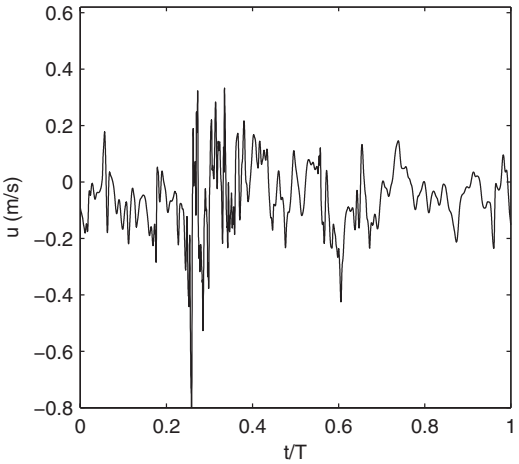

Fig. 15 Streamwise velocity versus time for one simulated cardiac cycle. Point is near the distal graft anastomosis ($x \approx 5$ mm) in the center of the vessel. Compare with Fig. 14.

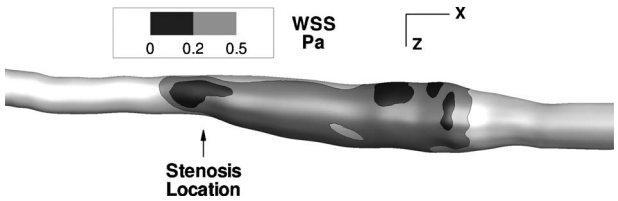

Fig. 16 Time-averaged WSS (in Pa) on the graft lumen for the scan at 1 month. The perspective has been rotated 90 deg counterclockwise about the *x*-axis compared with that in Fig. 7. Black color represents TAWSS<0.2 Pa, dark gray color represents 0.2 Pa<TAWSS<0.5 Pa, and light gray color represents TAWSS>0.5 Pa. The arrow indicates the future location of the stenosis ($x \approx -27$ mm).

in the recirculation region is the most discernible hemodynamic feature correlating with intimal thickening and the stenosis growth.

The TAWSS values in the first two scans in much of the patch recirculation zone is less than the threshold for "low" wall shear stress (<0.5 Pa) proposed by Jackson et al. [27]. Upon further examination of the TAWSS at 1 month, localized spots of even lower WSS (<0.2 Pa) were seen in the revised region. Figure 16 details the thresholds of low TAWSS at 1 month on the lumen the revised region. Although much of the patch region is subject to WSS <0.5 Pa, a localized area of WSS <0.2 Pa is observed to be coincident with the future site of the stenotic lesion. We therefore hypothesize that ≈0.2 Pa (between 0.15 Pa and 0.25 Pa) is a threshold for the production of clinically significant stenosis in lower extremity bypass grafts.

This fact also provides evidence of the role of localized secondary or "disturbed" flows in assisting the development of focal stenoses. This is a popular, although unproven, hypothesis [18]. We consider then that the low WSS is in part responsible for endothelial dysfunction, misregulation of the SMC in the media, and ultimately, intimal hyperplasia and stenosis [13,14].

Certainly additional factors beyond hemodynamics are related to the stenosis. For example, the proximal side of the stenosis at 16 months is subjected to elevated levels of shear stress (see Fig. 7). Yet if the intimal thickness is inversely proportional to the WSS, it begs the following question: why does the stenosis growth continue rather than stabilizing or regressing under the elevated shear stress? We speculate that additional physiological factors such as a localized loss of endothelial function or denudation due to the high levels of WSS resulting from the reduction in cross-sectional area are coadjuvant to the effect of low shear on IH. It has long been speculated that the injury sustained during the surgery to the graft induces a proliferative cellular response in the intima [12]. However, it has also long been speculated that the endothelium modulates this response when subjected to normal values of WSS [11]. Localized physiological abnormalities, in conjunction with localized hemodynamic factors (such as low WSS), may lead to biological deficiencies (such as decreased NO and prostacyclin production) and ultimately intimal hyperplasia [18].

High OSI was observed in the patch region, but the OSI may not provide additional insight into the flow dynamics. As stated previously, the OSI is often used as a measure of temporal variability in order to identify vascular regions susceptible to atherosclerosis. It has been shown by Lee and Steinman [33] that in the carotid bifurcation the OSI is, in general, a redundant measure of low WSS, i.e., regions of high OSI are correlated with regions of low WSS. Although this trend is seen in the scans at 1 and 6 months, the opposite is true in the scan at 16 months; high OSI in the dilated poststenotic region is related to high frequency velocity fluctuations and temporal shift in the jet stagnation point. But the dilated poststenotic region is still accompanied by high WSS due to the jet impingement. The OSI is of less utility when compared with TAWSS; one cannot independently distinguish the magnitude of the shear stress. Thus, a region with a high WSS and a high OSI may be falsely identified as susceptible to intimal hyperplasia.

Stenosis development is not seen in regions of high WSSG (i.e., >1000 Pa/m) such as the vessel segment proximal to the patch anastomosis. Likewise, distal to the flow separation in the flow recirculation, the WSSG is actually at its lowest values. The connection between WSSG and intimal thickening remains inconclusive.

Regarding the poststenotic dilatation, the ease with which PSD is created in animal models by ligation suggests mechanical factors are responsible for this phenomenon. Furthermore, the speed with which dilatation will recess after the removal of the ligation further suggests mechanical factors control a reversible signaling and remodeling process in the vessel wall. The poststenotic jet impingement and subsequent breakdown into high frequency fluctuations are an important hemodynamic factor that will influence the remodeling in this region. Roughly two families of theories have been proposed to explain the mechanical origins of PSD: that dilatation is "structural fatigue" from wall vibrations induced by high frequency turbulent pressure fluctuations, as suggested by Roach [37], or that dilatation is a relaxation of the vascular muscle triggered by abnormal shear stresses exerted on the endothelium [38].

These simulations have assumed a rigid lumen (and therefore wall stretch cannot be measured) but presumably the high frequency turbulent fluctuations would induce a palpable thrill due to the rapid temporal variations in pressure. The frequencies associated with the poststenotic velocity fluctuations are in a bandwidth associated with bruits or thrills. So, on the one hand, these results would be consistent with the hypothesis that the flow-induced wall vibration instigates the dilatation. But, on the other hand, the notion of "structural fatigue" is too simplistic given our current knowledge of active tissue remodeling. Instead, we may consider that the dilatation is a stretch mediated phenomenon. Given the evidence that stretch initiates a response in endothelial cells [10], the role of wall vibration in the remodeling cannot be neglected (albeit by a different mechanism than that considered in Ref. [37]). It is widely assumed that high shear stress does lead to reduced muscular tone in vascular grafts short term, in a NO-mediated response [18]. We must also certainly consider the role of the shear-stress-mediated endothelial response in the dilatation. Future studies are thus needed to determine the relative importance of stretch versus shear stress in PSD.

More systematic models of vessel growth and remodeling are needed in future computational studies to discern the relationship between local shear stress and stenosis development and to enhance our predictive capabilities. In particular, quantitative relationships between the time history of vessel quantities, such as intima-media thickness or lumen diameter, and their responses to mechanical stress, like those proposed by Jackson et al. [27], are needed. More frequent monitoring of grafts, particularly in the first 3 months postsurgery when the wall remodeling occurs at its fastest rate [7,19], are necessary to further elucidate the feedback process between changes in flow and lumen cross section. Likewise, additional models concerning the understanding of shear in endothelial NO production and the associated mass transfer process are also needed to differentiate the role of transient versus chronic vessel adaptation in graft patency.

5 Conclusions

This study presents the application of ultrasound image-based modeling to the study of peripheral artery graft remodeling and failure. Its availability, ease of use, and temporal resolution provide it with certain advantages over other image-based modeling modalities. The numerical simulations, coupled with the longitudinal patient scans, have the potential to reveal the complex hemodynamic features and their role in determining long-term mor-

phological remodeling and, more importantly, clinical outcomes. Our patient scans have revealed two significant remodeling features: the stenotic lesion, which ultimately caused graft failure, and the poststenotic dilatation. The simulations have further revealed complicated hemodynamic features: the flow separation and low shear recirculation zone distal to the stenosis and the poststenotic jet and high shear impingement. In vivo Doppler ultrasound velocity measurements also suggested the existence of these secondary flows. The simulations were also in qualitative agreement with the in vivo measurements. The focal nature of these flow features, and their concurrence with the wall remodeling, provides evidence of the secondary flows' specific role in the remodeling process. Moreover, we suggest a hypothesis that 0.2 Pa be considered a threshold for low WSS, which would be conducive to clinically significant stenoses. More frequent follow-up for patients with peripheral artery bypass grafts need to be carried out in future studies to validate the hypotheses formulated here for the relationship between hemodynamics and vessel wall remodeling.

Acknowledgment

This work has been supported in part by an R21 grant from NIDDK (Grant No. DK08-1823).

References

[1] Conte, M. S., 2006, "Results of Prevent III: A Multicenter, Randomized Trial of Edifolidge for the Prevention of Vein Graft Failure in Lower Extremity Bypass Surgery," J. Vasc. Surg., **43**(4), pp. 742–751.
[2] Goodney, P. P., Beck, A. W., Nagle, J., Welch, H. G., and Zwolak, R. M., 2009, "National Trends in Lower Extremity Bypass Surgery, Endovascular Interventions, and Major Amputations," J. Vasc. Surg., **50**(1), pp. 54–60.
[3] Mills, J. L., Bandyk, D. F., Gahtan, V., and Esses, G. E., 1995, "The Origin of Infrainguinal Vein Graft Stenosis: A Prospective Study Based on Duplex Surveillance," J. Vasc. Surg., **21**(1), pp. 16–25.
[4] Watson, H. R., Buth, J., Schroeder, T. V., Simms, M. H., and Horrocks, M., 2000, "Incidence of Stenoses in Femorodistal Bypass Vein Grafts in a Mulicentre Study," Eur. J. Vasc. Endovasc Surg., **20**, pp. 67–71.
[5] Owens, C. D., Rybicki, F. J., Wake, N., Schanzer, A., Mitsouras, D., Gerhard-Herman, M. D., and Conte, M. S., 2008, "Early Remodeling of Lower Extremity Vein Grafts: Inflammation Influences Biomechanical Adaptation," J. Vasc. Surg., **47**(6), pp. 1235–1242.
[6] Fillinger, M. F., Cronenwett, J. L., Besso, S., Walsh, D. B., and Zwolak, R. M., 1994, "Vein Adaption to the Hemodynamic Environment of Infrainguinal Grafts," J. Vasc. Surg., **19**, pp. 970–978.
[7] Owens, C. D., Wake, N., Jacot, J. G., Gerhard-Herman, M., Gaccionce, P., Belkin, M., Creager, M. A., and Conte, M. S., 2006, "Early Biomechanical Changes in Lower Exremity Vein Grafts—Distinct Temporal Phases of Remodeling and Wall Stiffness," J. Vasc. Surg., **44**(4), pp. 740–746.
[8] Galt, S. W., Zwolak, R. M., Wagner, R. J., and Gillbertson, J. J., 1993, "Differential Response of Arteries and Vein Grafts to Blood Flow Reduction," J. Vasc. Surg., **17**(3), pp. 563–570.
[9] Dobrin, P. B., 1995, "Mechanical Factors Associated With the Development of Intimal and Medial Thickening in Vein Grafts Subjected to Arterial Pressure," Hypertension, **26**, pp. 38–43.
[10] Lemson, M. S., Tordoir, J. H. M., Daemen, M. J. A. P., and Kitslaar, P. J. E. H. M., 2000, "Intimal Hyperplasia in Vascular Grafts," Eur. J. Vasc. Endovasc Surg., **19**, pp. 336–350.
[11] Kohler, T. R., Kirkman, T. R., Kraiss, L. W., Zierler, B. K., and Clowes, A. W., 1991, "Increased Blood Flow Inhibits Neointimal Hyperplasia in Endothelialized Vascular Grafts," Circ. Res., **69**, pp. 1557–1565.
[12] Bassiouny, H. S., White, S., Glagov, S., Choi, E., Giddens, D. P., and Zarins, C. K., 1992, "Anastomotic Intimal Hyperplasia: Mechanical Injury or Flow Induced," J. Vasc. Surg., **15**(4), pp. 708–717.
[13] Meyerson, S. L., Skelly, C. L., Curi, M. A., Shakur, U. M., Vosicky, J. E., Glagov, S., Christen, T., Gabbiani, G., and Schwartz, L. B., 2001, "The Effects of Extremely Low Shear Stress on Cellular Proliferation and Neointimal Thickening in the Failing Bypass Graft," J. Vasc. Surg., **34**(1), pp. 90–97.
[14] Jiang, Z., Wu, L., Miller, B. L., Goldman, D. R., Fernandez, C. M., Abouhamze, Z. S., Ozaki, C. K., and Berceli, S. A., 2003, "A Novel Vein Graft Model: Adaption to Differential Flow Environments," Am. J. Physiol. Heart Circ. Physiol., **286**, pp. 240–245.
[15] DePaola, N. Gimbrone, M. A., Jr., Davies, P. F., and Dewey, C. F., Jr., 1992, "Vascular Endothelium Responds to Fluid Shear Stress Gradients," Arterioscler., Thromb. Vasc. Biol., **12**, pp. 1254–1257.
[16] White, C. R., Haidekker, M., Bao, X., and Frangos, J. A., 2001, "Temporal Gradients in Shear, But Not Spatial Gradients, Stimulate Endothelial Cell Proliferation," Circulation, **103**, pp. 2508–2513.
[17] Carroll, G. T., McGloughlin, T. M., O'Keefee, L. M., and Callanan, A., 2009, "Realistic Temporal Variations of Shear Stress Modulate mmp-2 and mcp-1 Expression in Arteriovenous Vascular Grafts," Cell Mol Bioengr, **2**(4), pp. 591–605.
[18] Owens, C. D., 2010, "Adaptive Changes in Autogenous Vein Grafts for Arterial Reconstruction: Clinical Implications," J. Vasc. Surg., **51**(3), pp. 736–746.
[19] Leotta, D. F., Primozich, J. F., Beach, K. W., Bergelin, R. O., Zierler, R. E., and Strandness, D. E., Jr., 2003, "Remodeling in Peripheral Vein Graft Revisions: Serial Study With Three-Dimensional Ultrasound Imaging," J. Vasc. Surg., **37**(4), pp. 798–807.
[20] Loth, F., Fischer, P. F., and Bassiouny, H. S., 2008, "Blood Flow in End-to-Side Anastomoses," Annu. Rev. Fluid Mech., **40**, pp. 367–393.
[21] Lei, M., Archie, J. P., and Kleinsteuer, C., 1997, "Computational Design of a Bypass Graft That Minimizes Wall Shear Stress Gradients in the Region of the Distal Anastomosis," J. Vasc. Surg., **25**(4), pp. 637–646.
[22] Lei, M., Giddens, D. P., Jones, S. A., Loth, F., and Bassiouny, H., 2001, "Pulsatile Flow in and End-to-Side Vascular Graft Model: Comparison of Computations With Experimental Data," ASME J. Biomech. Eng., **123**, pp. 80–87.
[23] Walsh, M. T., Kavanagh, E. G., O'Brien, T., Grace, P. A., and McGloughlin, T., 2003, "On the Existence of an Optimum End-to-Side Junctional Geometry in Peripheral Bypass Surgery—A Computer Generated Study," Eur. J. Vasc. Endovasc Surg., **26**, pp. 649–656.
[24] O'Brien, T. P., Grace, P., Walsh, M., Burke, P., and McGloughlin, T., 2005, "Computational Investigations of a New Prosthetic Femoral-Popliteal Bypass Graft Design," J. Vasc. Surg., **42**, pp. 1169–1175.
[25] Moore, J. A., Steinman, D. A., Prakash, S., Johnston, K. W., and Ethier, C. R., 1999, "A Numerical Study of Blood Flow Patterns in Anatomically Realistic and Simplified End-to-Side Anastomoses," ASME J. Biomech. Eng., **121**, pp. 265–272.
[26] Giordana, S., Sherwin, S. J., Peiró, J., Doorly, D. J., Crane, J. S., Lee, K. E., Cheshire, N. J. W., and Caro, C. G., 2005, "Local and Global Geometric Influence on Steady Flow in Distal Anastomoses of Peripheral Bypass Grafts," ASME J. Biomech. Eng., **127**, pp. 1087–1098.
[27] Jackson, M., Wood, N. B., Zhao, S., Augst, A., Wolfe, J. H., Gedroyc, W. M. W., Hughes, A. D., Thom, S. A. M., and Xu, X. Y., 2009, "Low Wall Shear Stress Predicts Subsequent Development of Wall Hypertrophy in Lower Limb Bypass Grafts," Artery Res., **3**, pp. 32–38.
[28] Leotta, D. F., Primozich, J. F., Beach, K. W., Bergelin, R. O., Eugene, D., and Strandess, J., 2001, "Serial Measurement of Cross-Sectional Area in Peripheral Vein Grafts Using Three-Dimensional Ultrasound," Ultrasound Med. Biol., **27**(1), pp. 61–68.
[29] Ansys, Inc., 2009, ANSYS® FLUENT®, release 12.1 ed.
[30] Lee, S.-W., and Steinman, D. A., 2007, "On the Relative Importance of Rheology for Image-Based CFD Models of the Carotid Bifurcation," ASME J. Biomech. Eng., **129**(2), pp. 273–279.
[31] Womersley, J. R., 1955, "Method for the Calculation of Velocity, Rate of Flow and Viscous Drag in Arteries When the Pressure Gradient Is Known," J. Physiol., **127**, pp. 553–563.
[32] Cantón, G., Levy, D. I., and Lasheras, J. C., 2005, "Hemodynamic Changes Due to Stent Placement in Bifurcating Intracranial Aneurysms," J. Neurosurg., **103**(1), pp. 146–155.
[33] Lee, S.-W., Antiga, L., and Steinman, D. A., 2009, "Correlations Among Indicators of Disturbed Flow at the Normal Carotid Bifurcation," ASME J. Biomech. Eng., **131**(6), pp. 061013.
[34] He, X., and Ku, D. N., 1996, "Pulsatile Flow in the Human Left Coronary Artery Bifurcation: Average Conditions," ASMEJ. Biomech. Eng., **118**, pp. 74–82.
[35] Fung, Y. C., 1993, *Biomechanics: Mechanical Properties of Living Tissues*, Springer, New York.
[36] Stroud, J. S., Berger, S. A., and Saloner, D., 2000, "Influence of Stenosis Morphology on Flow Through Severely Stenotic Vessels: Implications for Plaque Rupture," J. Biomech., **33**, pp. 443–455.
[37] Roach, M. R., 1963, "An Experimental Study of the Production and Time Course of Poststenotic Dilatation in the Femoral and Carotid Arteries of Adult Dogs," Circ. Res., **13**, pp. 537–551.
[38] Ojha, M., and Langille, B. L., 1993, "Evidence that Turbulence Is Not the Cause of Poststenotic Dilatation in Rabbit Carotid Arteries," Arterioscler., Thromb., Vasc. Biol., **13**, pp. 977–984.